Advanced Materials Interfaces

ADVANCED MATERIALS INTERFACES Open Access

www.advmatinterfaces.de

RESEARCH ARTICLE OPEN ACCESS

Metastable Ordered Mesoporous *h*-$LuFeO_3$ Thin Films Prepared by Soft-Templating: Optical, Electronic, and Magnetic Properties

Christian Suchomski[1] | Christian Reitz[2] | Vipin Kumar[3] | Igor Djerdj[4] | Marcus Einert[3] | Torsten Brezesinski[2] | Bernd Smarsly[1]

[1]Institute of Physical Chemistry, Justus-Liebig-University Giessen, Giessen, Germany | [2]Institute of Nanotechnology, Karlsruhe Institute of Technology (KIT), Karlsruhe, Germany | [3]Surface Science Laboratory, Department of Materials and Earth Sciences, Technical University of Darmstadt, Darmstadt, Germany | [4]Department of Chemistry, Josip Juraj Strossmayer University of Osijek, Osijek, Croatia

Correspondence: Christian Suchomski (christian.suchomski@gmx.de) | Marcus Einert (meinert@surface.tu-darmstadt.de)

Received: 14 July 2025 | **Revised:** 14 November 2025 | **Accepted:** 7 December 2025

Keywords: diblock copolymer | EISA | mesoporosity | metastability | phase formation

ABSTRACT

A sol–gel-based soft-templating strategy for the synthesis of a hexagonal rare-earth orthoferrite and characterization of its structural, optical, electronic, and magnetic properties are reported. Specifically, the work aims to show that amphiphilic block copolymers as structure-directing agents (SDAs) are suitable for the production of metastable *h*-$LuFeO_3$, a phase that is not observed without SDA. The ability of the polymer SDA used herein to self-organize into superstructures while remaining compatible with inorganic building blocks, known as the evaporation-induced self-assembly process (EISA), resulted in a honeycomb-like network of open pores. In contrast to conventional epitaxy, it is demonstrated that the *h*-$LuFeO_3$ can be readily deposited as polycrystalline thin films on both silicon and quartz substrates by facile dip coating. The formation mechanism of the mesoporous material during calcination in air is investigated using various physicochemical characterization techniques. This revealed that certain reaction intermediates are produced that promote the formation of the hexagonal phase. Density functional theory calculations support the experimentally derived properties and further provide information on the electronic band structure. Overall, this study demonstrates a novel synthetic approach for producing ordered mesoporous and ferromagnetic $LuFeO_3$ thin films in the hexagonal rather than the orthorhombic phase due to the presence of a polymer SDA during synthesis.

1 | Introduction

During the last decades, materials science has been focused strongly on tailoring (phase) composition and structure of metal oxides to achieve desired properties. Equally challenging is the preparation of metastable compounds, which can be realized, among others, by solidification of undercooled melts or epitaxial growth [1, 2]. However, there is a lack of wet-chemical techniques to produce metastable phases/materials.

Hexagonal rare-earth orthoferrites (*h*-$RFeO_3$) represent a promising class of metastable materials exhibiting various technologically relevant properties, such as ferroelectricity or ferromagnetism at room temperature [3, 4]. Notably, they are promising candidates for application in spintronics, e.g., for the development of advanced memory devices. *h*-$RFeO_3$ (R = Y, Eu, Yb) materials were first synthesized in the 90s [5, 6], although the structurally related manganites (*h*-$RMnO_3$, R = Y, Ho–Lu) and aluminates (*h*-$RAlO_3$, R = Y, Eu–Er) with $P6_3cm$ and $P6_3/mmc$

structures, respectively, have already been known for many years [7, 8]. Despite the discovery, the low-temperature *h*-$RFeO_3$ phase received virtually no attention until Bossak and coworkers prepared thin films by metal-organic vapor-phase epitaxy (MOVPE) in 2004 [9].

The expectation of ferroelectric and magnetic ordering being present simultaneously in *h*-$RFeO_3$ films has renewed interest in these materials. Several synthesis methods can be employed to produce highly crystalline *h*-$RFeO_3$, including MOVPE [9], spray pyrolysis [6], container-less processing [10, 11], molecular beam epitaxy (MBE) [12, 13], pulsed laser deposition (PLD) [14, 15], or sol–gel routes [16–18]. Apart from these well-established methods, herein it is shown that the evaporation-induced self-assembly (EISA) process [19], extensively reported for the preparation of mesostructured materials in literature [20–23], can be used (to our knowledge for the first time) to produce honeycomb *h*-$LuFeO_3$ in film and powder form. Notably, the EISA-based soft-templating approach is an inexpensive and straightforward method to prepare self-assembling nanoarchitectures [19, 24, 25], such as ordered mesoporous metal oxides [26–29]. In this context, $CoFe_2O_4$ thin films, synthesized by the EISA method via dip coating [30] showed that ordered mesoporous networks exhibit unique magnetic properties. Specifically, the authors demonstrated a strong preference for out-of-plane magnetization due to buildup of in-plane tensile strain, along with relaxation of out-of-plane strain [30]. These properties are typically only observed for epitaxial thin films. The major advantage of the EISA approach, however, lies in the possibility to use and combine low-cost nitrate salts with amphiphilic block copolymer structure-directing agents (SDAs), for which mesoporous films with thicknesses of several hundred nanometers can be obtained by facile spin or dip coating, followed by calcination in air. Multifaceted physicochemical characterization revealed that $LuFeO_3$ indeed crystallizes in the hexagonal phase when heated at temperatures above 800°C under preservation of the nanostructured architecture.

2 | Results and Discussion

In the present work, the honeycomb-like structure was produced by a poly(ethylene-*co*-butylene)-*block*-poly(ethylene oxide) diblock copolymer, hereafter referred to as KLE [31], using an EISA process [19, 32]. In this process, the SDA forms a lyotropic mesophase, which is replicated by the inorganic building blocks [33]. Ferric and lutetium nitrate salts as inorganic precursors gave the best results in terms of phase purity and structural uniformity. Specifically, an isotropic solution was prepared by blending ethanol, 2-methoxyethanol, KLE, and the respective hydrated nitrate salts (see Experimental section, Supporting Information, for details). This solution was used to prepare films by dip coating onto silicon or quartz glass substrates. As mentioned above, the inorganic/organic species undergo self-assembly during solvent evaporation, leading to the formation of a mesostructured (amorphous) framework [34]. Thermal treatment was then performed to (i) stabilize the "wet" composite material by driving condensation (i.e., crosslinking of inorganic building blocks) at 130°C, (ii) induce degradation of the SDA above 250°C, and (iii) convert the glassy matrix into a single-phase rare-earth orthoferrite at temperatures close to 900°C.

The mesoporous morphology was probed using scanning electron microscopy (SEM), transmission electron microscopy (TEM), and atomic force microscopy (AFM). Figure 1a–c shows top-view SEM images of the KLE-templated $LuFeO_3$ thin films heated at temperatures ranging from 830°C to 910°C. At 830°C, a crack-free, honeycomb-like network of about 15 nm diameter pores is evident. Tapping-mode AFM (Figure 1d) confirmed the formation of a structurally robust architecture with a smooth top surface, i.e., a low root-mean-square (RMS) roughness. With increasing calcination temperature (Figure 1b), the crystalline domains grow, with the grains appearing to be elongated along the vertical direction, thereby slightly distorting the cubic arrangement of pores. As can be seen from Figure 1c, the initial ordering is largely lost by 910°C due to thermally induced grain growth (coarsening). At this temperature, the crystalline domains are somewhat larger than the (initial) pore walls, a mismatch resulting in restructuring and loss of the nanoscale periodicity. The cross-sectional SEM images shown in Figure S1 further corroborate that mesoporosity persists throughout the bulk of the $LuFeO_3$ thin films. This was also confirmed by TEM analysis (Figure 1e–h), demonstrating the mesoporous nature of the material heated at 910°C and the hexagonal phase formation. The latter is apparent from the selected-area electron diffraction (SAED) pattern presented in Figure 1g. It is noteworthy that powder material Figure S2 showed the same crystallization behavior; the (002) lattice spacing (d_{002} = 0.585 nm) is characteristic of the hexagonal phase with space group $P6_3cm$ [35].

To investigate the crystallization behavior of the KLE-templated $LuFeO_3$ thin films, especially the solid-solid conversion reactions and phase transformation during heating, various characterization techniques, including X-ray diffraction (XRD), Fourier-transform infrared (FTIR) spectroscopy, Raman spectroscopy, and thermogravimetric analysis coupled with mass spectrometry (TGA-MS) were employed. Both FTIR spectroscopy and TGA-MS analysis provide important information on the film composition at the beginning of the solidification process. However, for such experiments, around 100 mg of sample is required for obtaining reliable results. This relatively large amount corresponds to the active mass of tens to hundreds of thin films. Therefore, KLE-templated $LuFeO_3$ in powder form was prepared under virtually identical conditions and studied accordingly.

Figure 2a–c shows the respective data from temperature-dependent FTIR spectroscopy, XRD, and TGA-MS measurements. At first, the freshly prepared auburn-colored solution was spin coated onto a petri dish, followed by drying in air at room temperature for 24 h (solidification). The heating rate was set to 5°C min^{-1}, with aging steps at 130°C for 3 and 6 h at 300°C (condensation). Subsequently, the powder material was heated to either 450°C, 600°C, 750°C, 800°C, or 900°C under ambient conditions. The FTIR spectroscopy and TGA-MS data indicate that the nitrate salts are partially dehydrated, with vibrational bands appearing in the spectral region between 1700 and 700 cm^{-1}. For comparison, spectra collected from both the diblock copolymer KLE and the hydrated metal salts employed in this work are shown in Figures S3–S5, along with the corresponding band assignments in Tables S1–S5.

The isolated ("free") planar trigonal nitrate ion (NO_3^-) has D_{3h} symmetry and shows four types of vibrational modes, namely

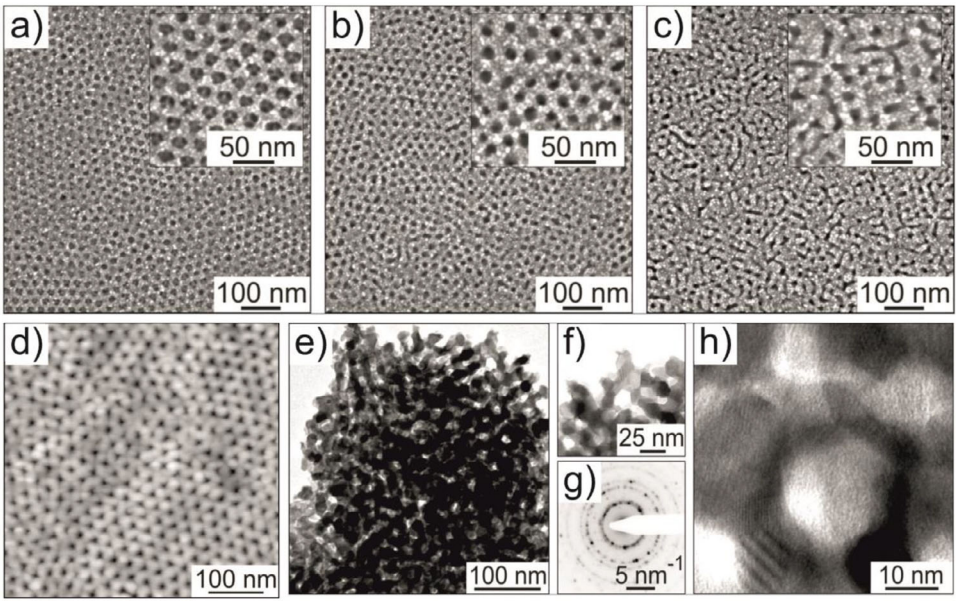

FIGURE 1 | Top-view SEM images of KLE-templated $LuFeO_3$ thin films heated at (a) 830°C, (b) 870°C, and (c) 910°C. (d) Tapping-mode AFM image (870°C), with the contrast covering height variations in the 0–6 nm range. (e, f, h) Bright-field TEM images (910°C) at different magnifications and (g) corresponding SAED pattern.

two non-degenerated ν_1 (NO symmetric stretch) and ν_2 (out-of-plane) as well as two doubly degenerated ν_3 (NO_2 asymmetric stretch) and ν_4 (NO_2 bend). However, if covalent or coordination bonds (i.e., monodentate, bidentate, or bridging ONO_2 groups) are present in a given metal nitrate compound/complex, the D_{3h} symmetry is lowered to either C_{2v} or C_s [36]. This leads to six fundamental modes of vibration, as reported by Gatehouse et al. [36]. Table S6 provides a summary of the observed frequencies and assignment of vibrational modes, while the established descriptions of nitrate vibrational modes are given in Tables S1 and S2.

Overall, two main conclusions can be drawn from the findings. First, it can be ascertained that after heat treatment at 300°C, the material is largely free of (crystal) water and the nitrate groups converted to oxynitrate [$MO_x(NO_3)_y$] and to a lesser extent to (di)oxy(mono)carbonate [$M_2O_{2+x}(CO_3)_{1-x}$] species (with M = Fe^{3+}, Lu^{3+}) [37, 38]. At this temperature and below, the formation of "$MONO_3$" represents an intermediate state. Ferric and lanthanide nitrates are known to dissolve in their own water of crystallization at temperatures above 60°C. This pathway is accompanied by dehydration and formation of hydroxy- and oxynitrate species (i.e., partial hydrolysis or thermolysis) [37]. Second, the SDA is not fully decomposed, as demonstrated by the presence of distinct C–H stretching modes (Figure S3 and Tables S3, S6). This is due to the preservation of the "PEB block" and agrees well with the TGA-MS data in Figure S6. It should be noted that KLE possesses a relatively high thermal stability up to 400°C, with about 40% of weight retained. In contrast, the commonly used Pluronic-type SDAs are pyrolyzed at temperatures below 300°C [39, 40]. It can be assumed that gaseous CO_2, as a thermal decomposition product of the PEO and PEB blocks, readily reacts with the in situ generated oxynitrate species to dioxymonocarbonates, such as $Fe_2O_2CO_3$ or $Lu_2O_2CO_3$. The latter have been shown to form in CO_2-rich environments [41, 42]. Lutetium dioxymonocarbonate, for example, is known to be stable over a broad temperature range and can be readily obtained by thermal combustion of organic precursors, such as acetates, oxalates, or related metal carboxylate compounds [43]. The emergence of $M_2O_{2+x}(CO_3)_{1-x}$ was observed at temperatures ≥300°C, as indicated by the FTIR spectroscopy data in Figure 2a. The gradual formation of CO_2 during calcination is apparent from the characteristic band at about 2336 cm^{-1} (ν_3, asymmetric stretch mode of CO_2). The progressive polymer degradation at elevated temperatures is accompanied by a steady increase in oxycarbonate formation, as proven by a series of FTIR spectra acquired at temperatures from 130 to 900°C (Table S6). The bands detected between 450°C and 750°C can be clearly assigned to carbonate vibrational modes (C_{2v} symmetry).

TGA-MS analysis revealed that both the nitrate and formed hydroxyl groups decompose between 130°C and 300°C to NO_x and H_2O (Figure 2c). However, the in situ generated oxynitrate species rather decompose toward 380°C, suggesting the formation of $LuONO_3$ as an intermediate [38]. Moreover, thermal and oxidative degradation products of the diblock copolymer KLE, e.g., C_2H_2 and CO_2, were also detected.

The crystallization behavior of the KLE-templated $LuFeO_3$ was studied in some detail by XRD. To this end, the sample was heated gradually to 900°C. No signs of crystallinity were found below 750°C. The lack of long-range ordering (amorphous nature) is apparent from the presence of a broad peak in the XRD pattern (Figure 2b). The latter was found to shift to around 33° 2Θ as the temperature increases from 130°C to 750°C, thus suggesting the formation of glassy $LuFeO_{2+x}(CO_3)_{1-x}$ as a kind of transition phase [43]. The stoichiometry parameter x (at 550°C) can be roughly estimated from the TGA-MS data. Because the SDA is completely combusted by 550°C (see MS signal of CO_2 in Figure 2c and Figure S6), the weight loss of about 3.6% from 550°C to 900°C corresponds to $x \approx 0.5$. In fact, some minor release of CO_2 was observed between 580°C and 780°C. The initially

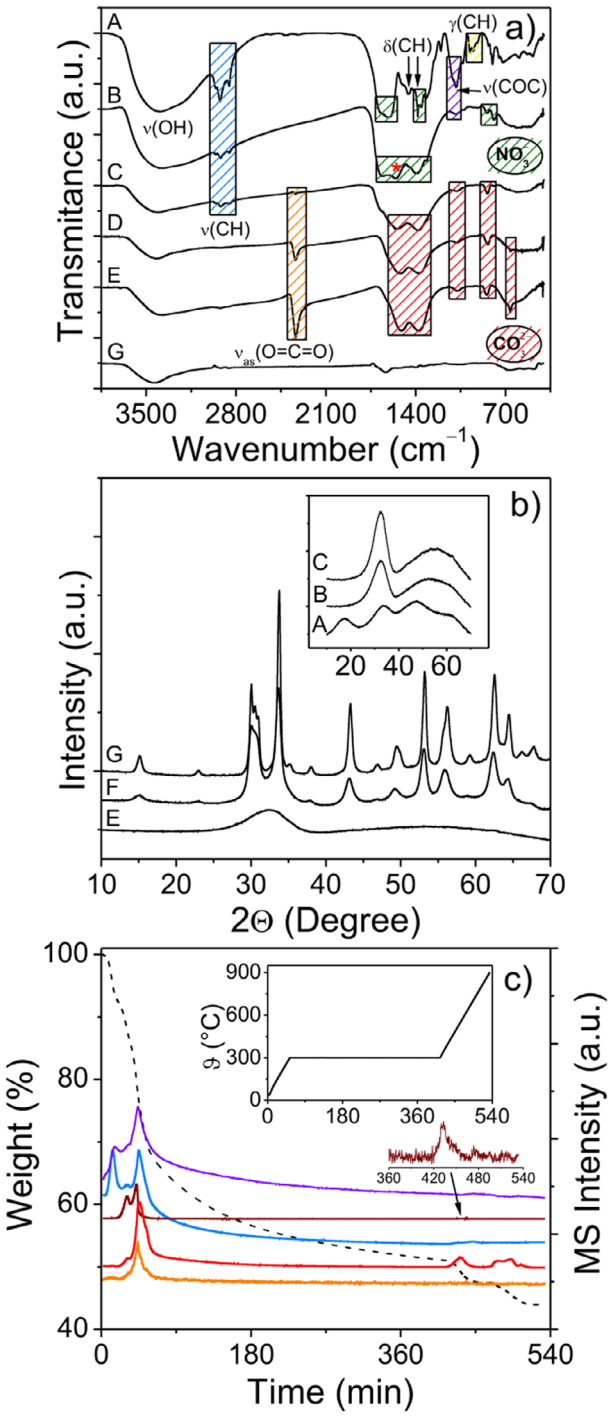

FIGURE 2 | (a) FTIR spectra and (b) XRD patterns of KLE-templated $LuFeO_3$ in powder form heated at 130°C (A), 300°C (B), 450°C (C), 600°C (D), 750°C (E), 800°C (F), and 900°C (G). The vibrational band marked with an asterisk indicates the presence of carbonates. (c) TGA-MS analysis in synthetic air (80% N_2 and 20% O_2) in the temperature range from 30°C to 900°C. The heating rate was set to 5°C min^{-1}. The dashed black line represents the TG curve. The MS analysis shows O_2 ($m/z = 32$) in purple, H_2O ($m/z = 18$) in blue, NO ($m/z = 30$) in brown, CO_2 ($m/z = 44$) in red, and C_2H_2 ($m/z = 26$) in orange. The solid black line in the inset displays the heating profile.

amorphous material crystallized in the hexagonal space group $P6_3cm$, as previously mentioned [11]. Considering both the XRD and MS data, the crystallization temperature was determined to be (780 ± 10)°C. The average grain size was calculated using the Scherrer equation to be (7.5 ± 2.0) nm at 800°C and (15.0 ± 2.0) nm at 900°C. Notably, no secondary phases, such as α-Fe_2O_3, *C*-type Lu_2O_3, *o*-$LuFeO_3$, or $Lu_3Fe_5O_{12}$, were detected, indicating the formation of single-phase, mesoporous *h*-$LuFeO_3$. Interestingly, in the absence of SDA, orthorhombic instead of hexagonal $LuFeO_3$ formed at a temperature of about 700°C (Figure S7). From this result, we conclude that the intermediate oxycarbonate phase plays an important role in the formation of *h*-$LuFeO_3$. This finding underscores that soft-templating can be used to produce unique crystallographic structures that cannot be formed in the sol–gel process without SDA (no oxycarbonate formation).

As proposed for epitaxially grown $LuFeO_3$ thin films [9], in the hexagonal structure with non-centrosymmetric space group $P6_3cm$ (C_{6v}^3), the elementary cell consists of six formula units, with Fe atoms being fivefold coordinated by a trigonal bipyramid of O atoms. The Lu atoms are eightfold-coordinated by O atoms in the form of a distorted dodecahedron and arranged between alternating layers of corner-sharing FeO_5 polyhedra [11]. In the basal (*ab*) plane, the FeO_5 bipyramids are slightly tilted with respect to the *c*-axis, as schematically shown in Figure 3a. By contrast, in the aristotype $P6_3/mmc$ structure, the FeO_5 bipyramids are not tilted and the Lu layers are planar and not buckled as in the lower-symmetry structure. Also, the Lu atoms are cubically coordinated by eight O atoms.

Figure 3b shows XRD patterns collected from a mesoporous *h*-$LuFeO_3$ thin film heated at temperatures between 830 and 910°C. As can be seen from this data, the material does in fact crystallize in the hexagonal system and is highly *c*-axis oriented, which is evident from the presence of distinct (00l) reflections. Re-addressing the results from the FTIR spectroscopy and TGA-MS investigations, the formation of $R_2O_{2+x}(CO_3)_{1-x}$ appears to play a crucial role in the crystallization behavior of *h*-$LuFeO_3$. Three structure types of rare-earth dioxymonocarbonates are described in the literature, namely tetragonal type-I ($I4/mmm$, C_{2v}^{20}), monoclinic type-Ia ($C2/c$, C_{2v}^6), and hexagonal type-II ($P6_3/mmc$, D_{6h}^4) [42]. Among these polymorphs, type-II $R_2O_2CO_3$ is the most stable phase; the others are metastable and transform into the high-temperature type-II phase at relatively low temperatures (≥400°C) [42]. Nevertheless, in all three polymorphic forms, the R^{3+} ions are eightfold coordinated by O^{2-} from the carbonate groups, $[R(CO_3)_4]^{5-}$, forming a distorted dodecahedron, as in the *h*-$RFeO_3$ phase. From the FTIR spectroscopy data, it can be construed that dodecahedral rare-earth sites also exist in the glassy $M_2O_{2+x}(CO_3)_{1-x}$, which appears to be beneficial to the preparation of *h*-$LuFeO_3$.

Although XRD is well suited for examining the bulk crystallinity, it can be insensitive to minor fractions of impurity phases, especially in nanocrystalline materials. Therefore, Raman spectroscopy measurements were carried out, aiming at ruling out

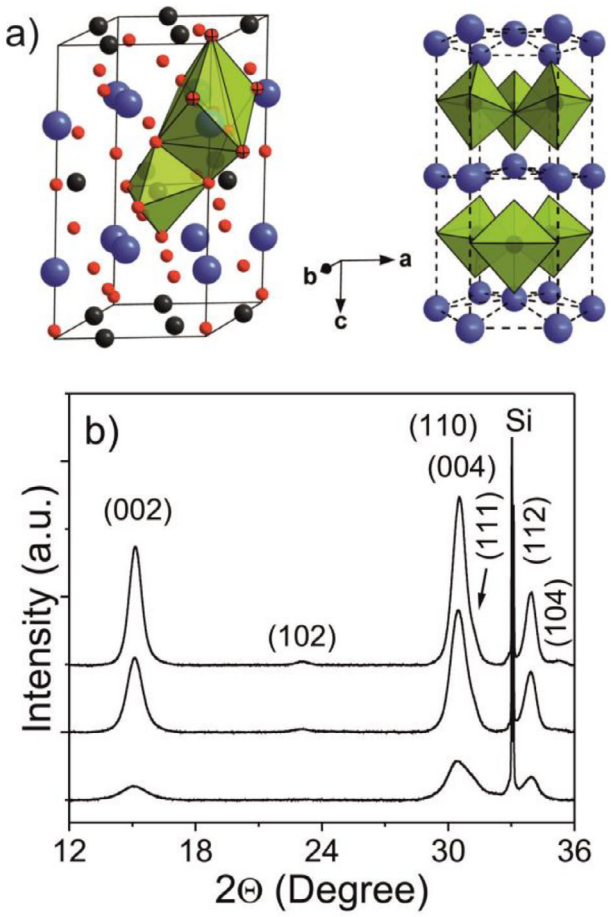

FIGURE 3 | (a) Scheme of the *h*-$LuFeO_3$ unit cell according to [11]. Lutetium atoms occupying the dodecahedral 2*a* and 4*b* sites are shown in blue, iron atoms on trigonal-bipyramidal 6*c* sites in black, and oxygen atoms on 2*a*, 4*b*, and 6*c* sites in red. Four additional oxygen atoms (black front ellipses) were added to illustrate the distorted cube. For the sake of clarity, all ions were drawn smaller (non-space-filling), and the relative size of oxygen atoms was reduced by a factor of 3.5. (b) XRD patterns of a 200 nm thick KLE-templated $LuFeO_3$ film heated at 830°C, 870°C, and 910°C (from bottom to top). The distinct peak at 33° 2Θ stems from the (100)-oriented silicon substrate used.

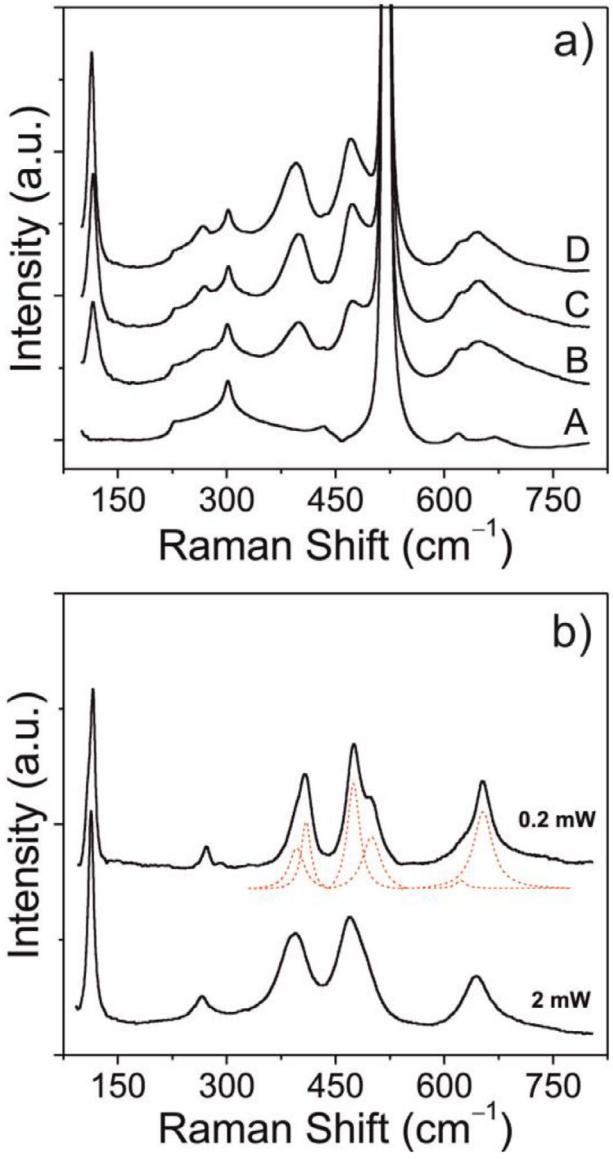

FIGURE 4 | (a) Raman spectra of KLE-templated $LuFeO_3$ thin films on (100)-oriented silicon substrate (A) heated at 830°C (B), 870°C (C), and 910°C (D). The appearance of bands at 232 cm^{-1} (2TA), 301 cm^{-1} (2TA), 433 cm^{-1} (2TA+2A), 470 cm^{-1} (2TO), 519 cm^{-1} (LO), 619 cm^{-1}, and 669 cm^{-1} (TO+TA) is due to Si-Si modes and indicates that the laser is capable of penetrating through the mesoporous material. (b) Raman spectra of KLE-templated $LuFeO_3$ in powder form heated at 900°C. Reference spectra of *o*-$LuFeO_3$ and *C*-type Lu_2O_3 are presented in Figure S8 for comparison. Note that some of the Raman bands were fitted with Lorentzian profiles, see dashed red curves.

the formation of secondary phases in the mesoporous *h*-$LuFeO_3$ thin films. Representative unpolarized Raman spectra of KLE-templated $LuFeO_3$ both in film and powder form, measured at room temperature, are shown in Figure 4a,b. For the powder sample, data was collected with different laser powers to achieve optimal separation of the broad Raman bands. According to group-theoretical considerations, the $P6_3cm$ structure of *h*-$LuFeO_3$ should give rise to 38 first-order Raman active modes ($9\times A_1$, $14\times E_1$, and $15\times E_2$). Their assignment is a challenging task (highly anisotropic material), as the phonon modes from different crystallographic directions are overlapping and can only be distinguished by polarized Raman scattering. Overall, seven and nine distinct Raman bands were detected for the film and powder samples, respectively. They were assigned based of literature data available for single-crystalline *h*-$LuMnO_3$ [44] and are given in Table 1. Specifically, Raman bands were observed at 114, 267, 373, 395, 470, 495, and 645 cm^{-1} for the thin films. The lack of bands is not surprising and can be understood in terms of finite-size effects (phonon confinement), which often results in line broadening and vanishing of phonon modes due to decreasing scattering intensity [45, 46]. Note that some modes are likely temperature-sensitive and can be only detected in low-temperature experiments, as shown for various *h*-$RMnO_3$ (R = Er, Y, Yb, Lu) materials, for example [47–50]. By changing the Nd:YAG laser power from 2 to 0.2 mW ($\lambda_{excitation}$ = 532 nm), both minor blue shifts of band positions and improved peak resolution were noticed. However, this strategy only worked for the powder material. Regardless, both the XRD and Raman spectroscopy

TABLE 1 | Raman bands and mode assignments for various *h*-$LuFeO_3$ materials.

	h-$LuFeO_3$			*h*-$LuMnO_3$ [45]	
No.	**Film (2 mW) (cm^{-1})**	**Powder (2 mW) (cm^{-1})**	**Powder (0.2 mW) (cm^{-1})**	**Single crystal (cm^{-1})**	**Assignment**
1	114	113	115	121	A_1
2	267	266	272	266	A_1
3	—	—	291	301/309	A_1/E_2
4	373	391	396	380	E_1
5	395	391	409		
6	470	469	475	472	A_1
7	495	491	500		
8	—	—	623	642	E_1
9	645	646	653	689	A_1

results provide profound evidence that the formation of impurity phases during high-temperature calcination can be excluded.

To gain insight into the surface and bulk chemical composition, band structure, and magnetic properties of the KLE-templated *h*-$LuFeO_3$ thin films, X-ray photoelectron spectroscopy (XPS), time-of-flight secondary ion mass spectrometry (ToF-SIMS), UV-vis spectroscopy, and superconducting quantum interference device (SQUID) measurements were conducted on the mesoporous material. In addition, density functional theory (DFT) calculations were carried out.

Detailed knowledge of the band gap energy (E_g) is required for potential applications in photoelectrochemical devices [51]. To determine the optical band gap, the equation $\alpha h\nu = \text{const}\ (h\nu - E_g)^n$ [describing the absorption coefficient (α) as a function of photon energy of incident light ($h\nu$)] can be exploited [52]. The type of optical transition, i.e., either direct or indirect, is given by the exponent n. Figure 5a shows Tauc plots for direct and indirect transitions in the KLE-templated *h*-$LuFeO_3$ thin films. The latter samples have a light orange to yellow color at room temperature. In the visible range between 800 and 400 nm (see absorbance spectra in Figure S9) two maxima at about 530 nm (~2.34 eV) and 430 nm (~2.88 eV) were observed. According to literature reports, they arise from electric dipole allowed oxygen-to-iron (O 2*p* to Fe 3*d*) charge-transfer transitions and are likely combined with spin-forbidden *d*-*d* transitions involving high-spin Fe^{3+} ions (e.g., $^6A_1 \rightarrow {}^4A_1$ and/or $^6A_1 \rightarrow {}^4A_2, {}^4E$) on trigonal bipyramidal sites [53, 54]. Interestingly, an indirect transition around 1.25 eV was detected in the low-energy infrared region, representing a 3*d* crystal-field transition, in agreement with theoretical predictions by Pavlov et al. [53]. Note that formally spin-forbidden *d*-*d* transitions may occur in magnetically coupled iron sublattices through antiferromagnetic interactions between adjacent Fe^{3+} ions [55]. The intensity of these transitions can be up to several orders of magnitude weaker compared to ligand-to-metal charge-transfer transitions. The band gap energy was determined from the data for the direct transition to be (1.9 ± 0.1) eV, which is in reasonable agreement with reported literature values [54]. The latter energy was determined by extrapolating the linear part of the curve to zero. However, ab initio band-structure calculations by Wang et al. for defect-free *h*-$LuFeO_3$ suggest a substantially lower value of 1.35 eV (~918 nm) and further a band gap structure of both direct and indirect nature [54]. Therefore, we also estimated the indirect band gap energy [(1.8 ± 0.1) eV]. In light of these findings, the mesoporous material can be categorized as a charge-transfer insulator [56].

To compare the experimentally derived data for the (opto)electronic properties with the electronic band structure, DFT calculations using the wave technique implemented in the Vienna ab initio simulation package (VASP) were performed [57]. It has been reported that the optical band gap energy of Fe-containing oxides differs significantly from the actual electronic band gap energy, primarily due to formation of polaron defect states [58]. The *h*-$LuFeO_3$ phase with space group $P6_3cm$ was referenced from previous work done by Magome et al. [11]. The lattice constants were re-optimized to a = 5.94 Å, b = 5.94 Å, and c = 11.66 Å. Figure 5b shows the band diagram of the crystal structure along the high-symmetry points of the Brillouin zone, calculated with an effective U value (U_{eff}) of 6.0 eV, providing a good match with the ab initio calculations by Wang et al. for defect-free *h*-$LuFeO_3$ [54]. The underlying calculations yield an indirect band gap energy of 1.20 eV (K − Γ) and a direct band gap energy of 1.41 eV (Γ − Γ), as indicated in Figure 5b. The electronic structure presented here is similar to that described in previous works by Han et al. [59] and Holinsworth et al. [60], with the notable difference that the top of the valence band is located at the K point rather than the Γ or A points. *h*-$LuFeO_3$ is found to exhibit an indirect band gap, contrary to previous studies that characterized it as a direct band gap material [60]. However, our current calculations are consistent with the findings of Melo et al. [61], who also reported on an indirect band gap of 1.03 eV (K − Γ) and a direct band gap of 1.06 eV (Γ − Γ) in non-collinear calculations with U_{eff} = 4.0 eV. The valence bands are situated nearer to the Fermi level than the conduction band lines, a trend also noted in the literature [61]. Our calculations with U_{eff} = 6.0 eV for the Fe element yielded a band gap that more closely matches the experimental results, showing (in the infrared region) an indirect transition at 1.20 eV (see also Figure S10), which is ascribed to a 3*d* crystal-field transition, in agreement with other studies [53]. However, the discrepancy between the

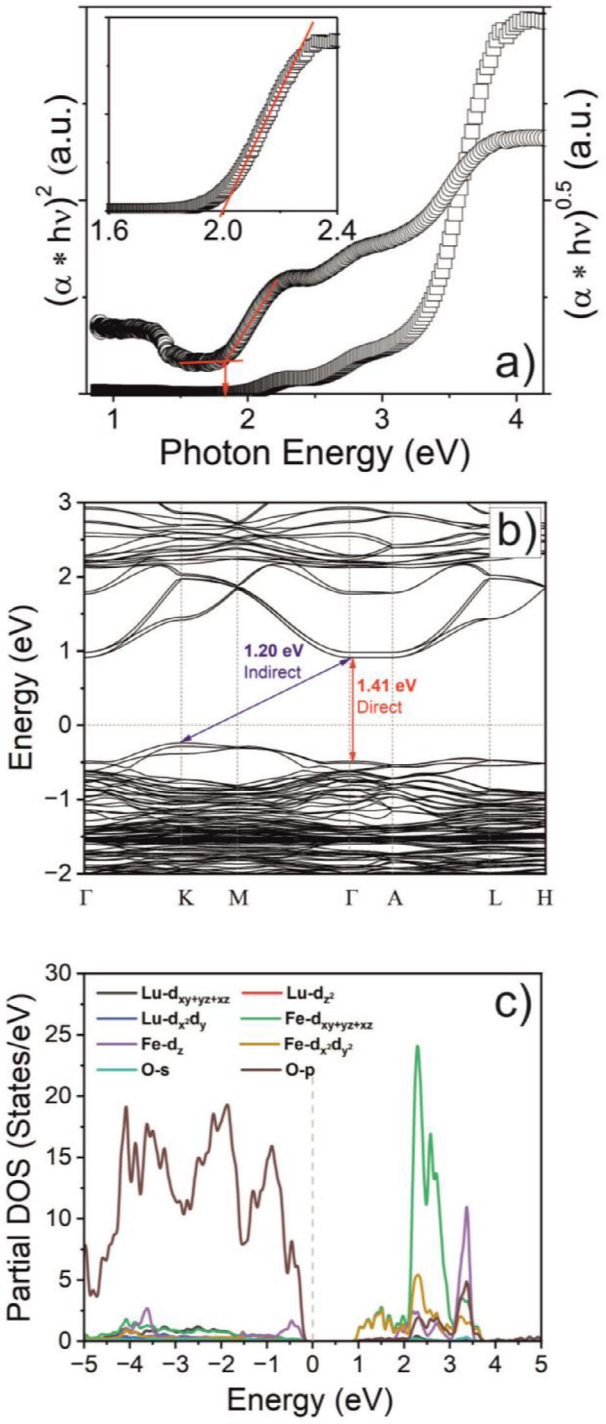

FIGURE 5 | (a) Tauc plots for direct (□) and indirect (○) optical transitions in KLE-templated $LuFeO_3$ thin films heated at 910°C. (b) Electronic band structure of *h*-$LuFeO_3$ along the high symmetry path directions in the Brillouin zone. (c) Total partial density of states of the *h*-$LuFeO_3$ phase for all elements. The energy distributions of Lu *d*, Fe *d*, O *s*, and O *p* states are illustrated.

experimental band gaps (1.9 eV direct, 1.8 eV indirect) and the DFT+U calculated ones (1.4 eV direct, 1.2 eV indirect) is expected after the +U correction also, as GGA-PBE-based methods are known to underestimate band gaps. The Hubbard U term improves the description of localized electron states, but it does not fully resolve the limitations of standard functionals in treating exchange-correlation effects. Further methods, such as hybrid functional HSE06 or GW calculations, are scope of perspective investigations. Therefore, we mainly focused on understanding the qualitative electronic structure and trends. For this purpose, theDFT+U method was used for computationally efficiency and has also been reported in previous work by Li et al. [62]. The partial density of states (PDOS) presented in Figure 5c elucidates the contributions of individual orbitals near the Fermi level. Specifically, the O *p* orbitals strongly contribute to the valence band, while the Fe $d_{xy+yz+xz}$ orbitals exhibit dominant contributions in the conduction band.

The chemical composition and oxidation states of the near-surface elements of the mesoporous material were probed using XPS. Figure 6a presents the survey spectrum, exhibiting photoemission lines of Lu, Fe, O, and C, as expected. High-resolution XP spectra revealed the spin-orbital splitting of Fe 2*p* at 710.6 eV ($2p_{3/2}$) and 724.8 eV ($2p_{1/2}$), with satellite peaks appearing at binding energies of 718–723 and 730–734 eV (Figure 6b), thus indicating the presence of Fe^{3+} [32, 63, 64]. The photoemission line of the Fe 3*p* state was identified at a lower binding energy of 55.8 eV. The Lu 4*d* core-level region showed peaks at 195.1 eV ($4d_{5/2}$) and 205.4 eV ($4d_{3/2}$) (Figure 6c), characteristic of Lu^{3+} [65]. In addition, the spin-orbital splitting of Lu 4*f* led to the appearance of peaks at 7.1 and 8.4 eV for the $4f_{7/2}$ and $4f_{5/2}$ contributions, respectively [66]. Overall, the XPS data corroborate the above results.

ToF-SIMS measurements were also conducted to learn about the elemental distribution in the bulk of the KLE-templated *h*-$LuFeO_3$ thin films. Figure 7a shows the profiles for Si^+, Fe^+, and Lu^+ as a function of depth from the top surface to the (silicon) substrate. The film thickness was determined by profilometry after ion sputtering. From this data, it appears that iron is slightly enriched at the top surface, while lutetium is depleted, likely due to segregation effects. Similar findings have been made for chemically different but structurally related metal oxide films [67, 68]. Hence, ToF-SIMS confirms that both iron and lutetium are uniformly distributed throughout the bulk.

To characterize the Brunauer-Emmett-Teller (BET) surface area of the *h*-$LuFeO_3$ thin films, an N_2-physisorption analysis was performed, as shown in Figure 7b, taking into account the film dimension, porosity, and density. The specific surface area was determined to be approximately 140 $m^2\ g^{-1}$, which is consistent with values found for other KLE-templated metal oxide thin films [26, 67]. The hysteresis loops can be attributed to the gas adsorption behavior that occurs exclusively in mesoporous networks (multilayer adsorption followed by pore condensation) [69]. This is further confirmed by the cross-sectional SEM images in Figure S1, clearly showing that the bulk structure consists of a mesoporous framework (through-pore structure) that allows good accessibility for gaseous species.

The magnetic behavior of the *h*-$LuFeO_3$ thin films was investigated by SQUID magnetometry using a Quantum Design MPMS-XL5 system. Figure 8 shows typical out-of-plane zero-field-cooled (ZFC)/field-cooled (FC) curves acquired over the temperature range of 5–380 K. These measurements were performed after cooling the samples to liquid helium temperature (T = 4.2 K) and demonstrate to what extent the thermal energy affects the

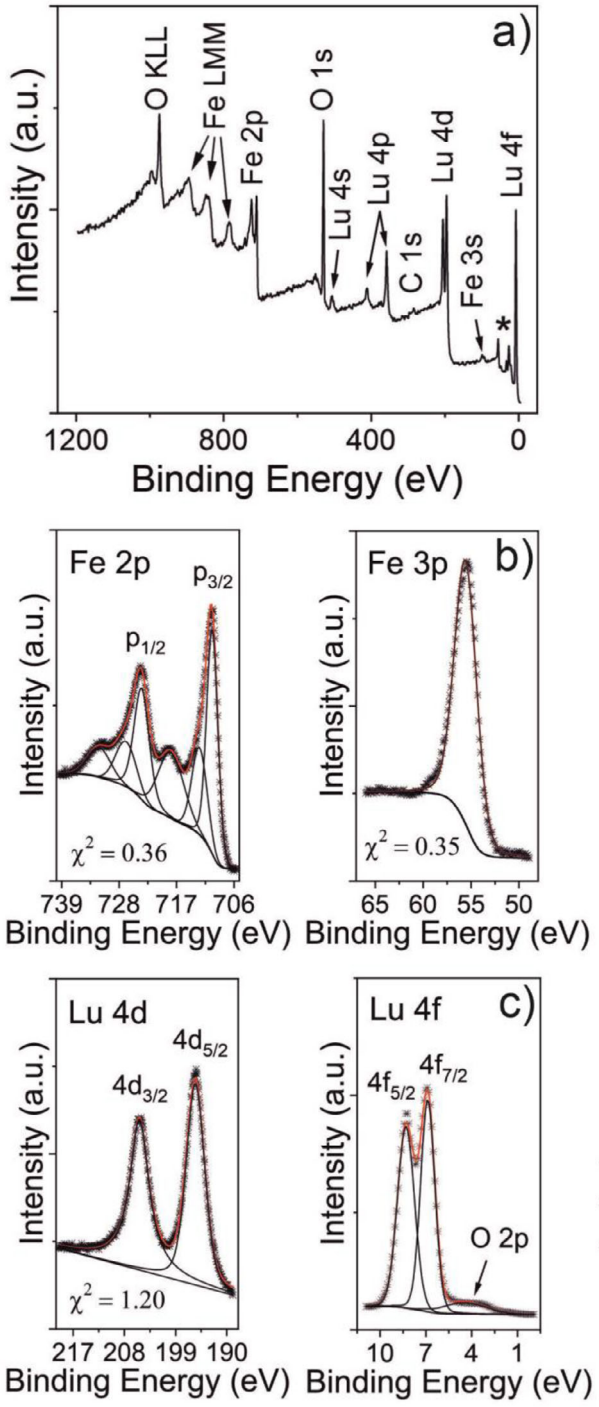

FIGURE 6 | (a) XP survey spectrum of KLE-templated $LuFeO_3$ thin films heated at 910°C. The asterisk denotes the Fe 3*p*, O 2*s*, and Lu 5*p* core-level regions at low binding energies. Detail spectra of the (b) Fe 2*p* and Fe 3*p* and (c) Lu 4*d* and Lu 4f core levels. Solid black lines represent fits to the data and those in red are the sum of peak fits.

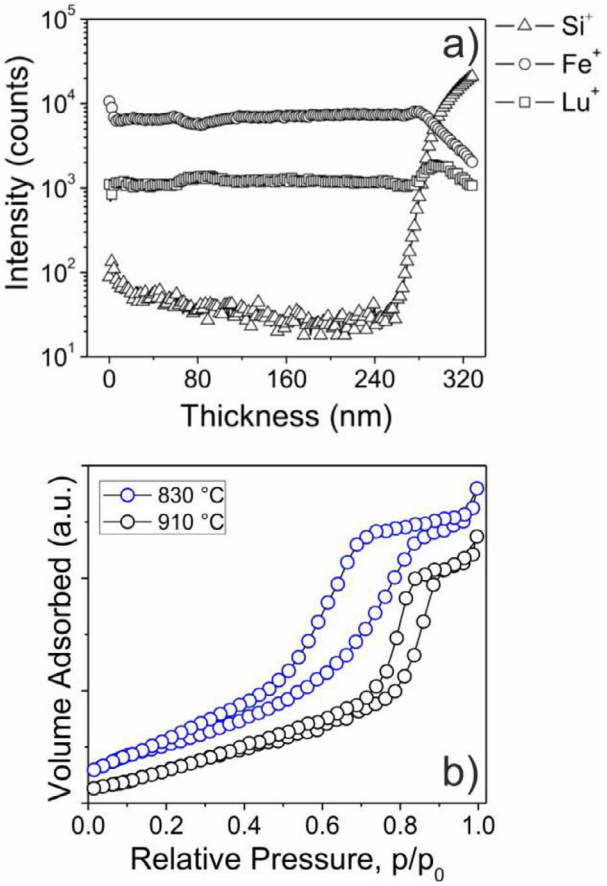

FIGURE 7 | (a) TOF-SIMS depth profile of a KLE-templated $LuFeO_3$ thin film on (100)-oriented silicon substrate heated at 910°C showing the distribution of Fe^+ (○), Lu^+ (□), and Si^+ (△). (b) N_2-adsorption/desorption isotherms for (500 ± 50) nm thick KLE-templated $LuFeO_3$ films with a total area of approximately 46 cm^2 after heating at 830°C (blue) and 910°C (black).

dc magnetization (*M*). From the ZFC and FC curves, which were measured at static magnetic fields of both 1 and 5 kOe, it is apparent that the mesoporous material exhibits ferromagnetic behavior and undergoes two distinct transitions at T_{SR1} = (125 ± 5) K and T_{SR2} = (325 ± 5) K at 5 kOe. These transitions can be attributed to a spin reorientation because of competing ferromagnetic states (driven by magnetic anisotropy), i.e., a spin reversal along the *c*-axis. The spin reversal at T_{SR1} has also been observed by neutron diffraction experiments conducted on 60 nm thick *h*-$LuFeO_3$ films [4]. A slight shift from (125 ± 5) K to (85 ± 5) K was found for smaller field strengths, likely due to some anisotropy of the ferromagnetic component. In principle, the mesoporous *h*-$LuFeO_3$ thin films contain magnetic Fe^{3+} ([Ar] $3d^5 4s^0$) and nonmagnetic Lu^{3+} ([Xe] $4f^{14} 5d^0 6s^0$) ions. Their ferromagnetic behavior is determined by antisymmetric Fe—O—Fe Dzyaloshinskii-Moriya exchange interactions [70, 71], similar to materials such as α-Fe_2O_3 [72], $FeBO_3$ [73], or *o*-$RFeO_3$ [74], involving slightly canted spins of the triangular sublattice on the *ab* plane along the out-of-plane direction [56, 75]. Unfortunately, the Curie temperature could not be determined, as it exceeded the temperature range of the equipment used. However, as evident, the material retains its long-range magnetic ordering up to temperatures of at least 380 K, in agreement with literature results [4]. The significantly higher spin-ordering temperature compared to *h*-$RMnO_3$ (R = Y, Yb, Lu; $T_N \leq 90$ K) [76] materials is reasonable because in Fe-based compounds, such as $BiFeO_3$ and *o*-$RFeO_3$, much stronger Fe—O—Fe exchange interactions are present and the contribution of five (thermally robust) 3*d* electrons per Fe atom with high-spin configuration dominates. Note that the strength of the anisotropic exchange

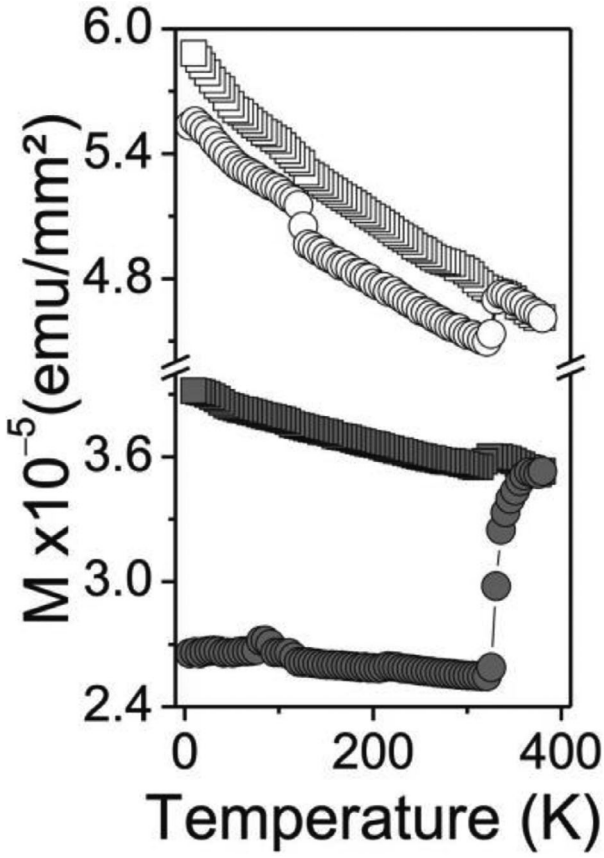

FIGURE 8 | ZFC (○)/FC (□) curves collected from a KLE-templated $LuFeO_3$ thin film heated at 910°C, with the plane of the substrate oriented perpendicular to the external magnetic field (out-of-plane direction) at 1 kOe (filled symbols) and 5 kOe (empty symbols).

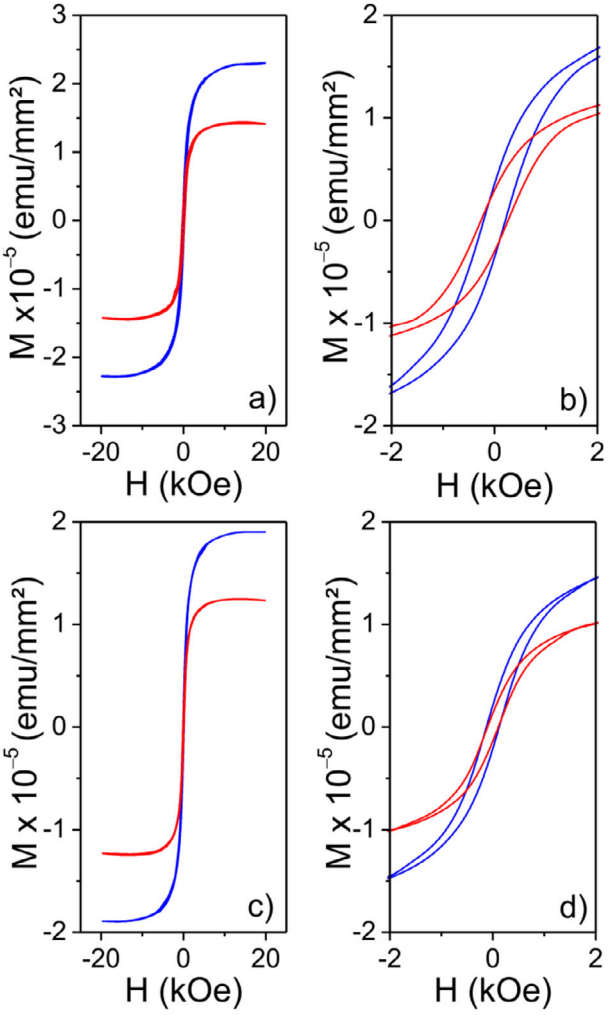

FIGURE 9 | In-plane (red) and out-of-plane (blue) magnetic properties of the KLE-templated $LuFeO_3$ thin films heated at 910°C. Hysteresis curves measured at (a, b) 5 K and (c, d) 300 K.

interaction has been shown to strongly depend on both the magnetic moment of the transition metal (Fe, Cr, Mn, etc.) and the bond angle and length.

To examine the coercivity (H_C) as a function of temperature, hysteresis curves (out-of-plane magnetization isotherms) were measured, as shown in Figure S11. The data clearly demonstrates that the films are ferromagnetic at room temperature and show no signs of superparamagnetism. Moreover, the material can be saturated at any temperature by a magnetic field of less than 10 kOe. Also, the shape of the hysteresis loops, as presented in Figure 9a–d, is typical of soft ferromagnets. The H_C values were determined to be 210 and 125 Oe (out-of plane; blue curves) and 265 and 105 Oe (in-plane; red curves) at 5 and 300 K, respectively. Overall, the KLE-templated *h*-$LuFeO_3$ thin films were found to exhibit characteristics of a ferromagnet at room temperature, with soft-magnetic properties.

3 | Conclusions

In this study, the preparation of metastable *h*-$LuFeO_3$ in film and powder form by soft-templating is reported. Samples having a high degree of pore ordering were successfully produced in the hexagonal instead of the orthorhombic phase commonly observed by using an amphiphilic poly(ethylene-*co*-butylene)-*block*-poly(ethylene oxide) diblock copolymer as structure-directing agent. The crystallization behavior of the hexagonal phase was probed using XRD, along with Raman and FTIR spectroscopy, as well as TGA-MS. Notably, the formation of $Lu_2O_{2+x}(CO_3)_{1-x}$ was found crucial to the synthesis of single-phase *h*-$LuFeO_3$ at temperatures above 800°C. Aside from that, the structural, optical, electronic, and magnetic properties of the ordered mesoporous thin films were thoroughly studied, among others, by electron microscopy, UV-vis spectroscopy, and SQUID magnetometry. Interestingly, they were found to be ferromagnetic at room temperature, with a preferred out-of-plane magnetization. The latter seems to be related to the strong texturing, which helps to overcome the shape anisotropy. Overall, this work represents an intriguing design concept for the preparation of mesoporous *h*-$LuFeO_3$ thin films (and probably also related hexagonal rare-earth orthoferrites) with unique physicochemical properties for application in various areas of materials science.

Acknowledgements

The authors thank Jan Haetge, Daniel Reppin, Zvonko Jagličić, and Thomas Leichtweiss for assistance in materials characterization. Financial support by the Fonds der Chemischen Industrie im Verband der Chemischen Industrie through a Chemiefonds fellowship (CR), the German Academic Exchange Service (TB), and the Federal Ministry of Research, Technology and Space (BMFTR) within the project TWOB under award no. 033RC036 (ME and VK) is acknowledged.

Open access funding enabled and organized by Projekt DEAL.

Conflicts of Interest

The authors declare no conflicts of interest.

Data Availability Statement

The data that support the findings of this study are available from the corresponding author upon reasonable request.

References

1. D. M. Herlach, "Metastable Materials Solidified From Undercooled Melts," *Journal of Physics: Condensed Matter* 13 (2001): 7737.

2. A. Kaul, O. Gorbenko, M. Novojilov, et al., "Epitaxial Stabilization—A Tool for Synthesis of New Thin Film Oxide Materials," *Journal of Crystal Growth* 275 (2005): e2445–e2451.

3. Y. K. Jeong, J.-H. Lee, S.-J. Ahn, et al., "Structurally Tailored Hexagonal Ferroelectricity and Multiferroism in Epitaxial $YbFeO_3$ Thin-film Heterostructures," *Journal of the American Chemical Society* 134 (2012): 1450–1453.

4. W. Wang, J. Zhao, W. Wang, et al., "Room-temperature Multiferroic Hexagonal $LuFeO_3$ Films," *Physical Review Letters* 110 (2013): 237601.

5. O. Yamaguchi, H. Takemura, M. Yamashita, and A. Hayashida, "Formation of Yttrium Iron Oxides Derived From Alkoxides," *Journal of the Electrochemical Society* 138 (1991): 1492.

6. Y. Mizoguchi, H. Onodera, H. Yamauchi, M. Kagawa, Y. Syono, and T. Hirai, "Mössbauer Spectra and Magnetic Susceptibilities of Ultrafine Hexagonal $RFeO_3$ (R≠ Eu, Yb) Particles Formed by the Spray Inductively Coupled Plasma Technique," *Materials Science and Engineering: A* 217 (1996): 164–166.

7. F. Bertaut and J. Mareschal, "Physique Des Solides-Un Nouveau Type De Structure Hexagonale-AITO3 (T= Y, EU, GD, TB, DY, HO, ER)," *Comptes Rendus Hebdomadaires Des Seances De L Academie Des Sciences* 257 (1963): 867.

8. H. L. Yakel Jnr, W. C. Koehler, E. F. Bertaut, and E. F. Forrat, "On the Crystal Structure of the Manganese (III) Trioxides of the Heavy Lanthanides and Yttrium," *Acta Crystallographica* 16 (1963): 957–962.

9. A. A. Bossak, I. E. Graboy, O. Y. Gorbenko, et al., "XRD and HREM Studies of Epitaxially Stabilized Hexagonal Orthoferrites $RFeO_3$ (R= Eu–Lu)," *Chemistry of Materials* 16 (2004): 1751–1755.

10. M. S. Vijaya Kumar, K. Kuribayashi, and K. Kitazono, "Effect of Oxygen Partial Pressure on the Formation of Metastable Phases From an Undercooled $YbFeO_3$ Melt Using an Aerodynamic Levitator," *Journal of the American Ceramic Society* 92 (2009): 903–910.

11. E. Magome, C. Moriyoshi, Y. Kuroiwa, A. Masuno, and H. Inoue, "Noncentrosymmetric Structure of $LuFeO_3$ in Metastable state," *Japanese Journal of Applied Physics* 49 (2010).

12. J. A. Mundy, C. M. Brooks, M. E. Holtz, et al., "Atomically Engineered Ferroic Layers Yield a Room-temperature Magnetoelectric Multiferroic," *Nature* 537 (2016): 523–527.

13. J. A. Moyer, R. Misra, J. A. Mundy, et al., "Intrinsic Magnetic Properties of Hexagonal $LuFeO_3$ and the Effects of Nonstoichiometry," *APL Materials* 2 (2014).

14. B. Biswas, F. Stramaglia, E. V. Pomjakushina, T. Lippert, C. A. F. Vaz, and C. W. Schneider, "Room Temperature Dy Spin-Flop Switching in Strained $DyFeO_3$ Thin Films," *Advanced Materials Interfaces* 12 (2025): 2400938.

15. B. Biswas, P. Naumov, F. Motti, et al., "Correlation of Structural and Magnetic Properties of $RFeO_3$ (R = Dy, Lu)," *Physical Review Materials* 8 (2024): 84404.

16. Y. Masuda, S. Hosokawa, and M. Inoue, "Combustion Activities of the Ru Catalysts Supported on Hexagonal $YbFeO_3$," *Journal of the Ceramic Society of Japan* 119 (2011): 850–854.

17. T. Nishimura, S. Hosokawa, Y. Masuda, K. Wada, and M. Inoue, "Synthesis of Metastable Rare-earth–iron Mixed Oxide With the Hexagonal Crystal Structure," *Journal of Solid State Chemistry* 197 (2013): 402–407.

18. A. Pakalniškis, D. O. Alikin, A. P. Turygin, et al., "Crystal Structure and Concentration-Driven Phase Transitions in Lu1−xScxFeO3 (0≤ x≤ 1) Prepared by the Sol–Gel Method," *Materials* 15 (2022): 1048.

19. C. J. Brinker, Y. Lu, A. Sellinger, and H. Fan, "Evaporation-induced Self-assembly: Nanostructures Made Easy," *Advanced Materials* 11 (1999): 579–585.

20. P. Yang, D. Zhao, D. I. Margolese, B. F. Chmelka, and G. D. Stucky, "Generalized Syntheses of Large-pore Mesoporous Metal Oxides With Semicrystalline Frameworks," *Nature* 396 (1998): 152–155.

21. G. J. A. A. Soler-Illia, C. Sanchez, B. Lebeau, and J. Patarin, "Chemical Strategies to Design Textured Materials: From Microporous and Mesoporous Oxides to Nanonetworks and Hierarchical Structures," *Chemical Reviews* 102 (2002): 4093–4138.

22. A.-H. Lu and F. Schüth, "Nanocasting: A Versatile Strategy for Creating Nanostructured Porous Materials," *Advanced Materials* 18 (2006): 1793–1805.

23. D. Gu and F. Schüth, "Synthesis of Non-siliceous Mesoporous Oxides," *Chemical Society Reviews* 43 (2014): 313–344.

24. T. Kimura, "Smart Synthesis of Highly Porous Metal Oxide Powders With the Self-assembly of Amphiphilic Organic Compounds," *Dalton Transactions* 53 (2024): 12434–12441.

25. M. Einert, M. Mellin, N. Bahadorani, C. Dietz, S. Lauterbach, and J. P. Hofmann, "Mesoporous high-entropy Oxide Thin Films: Electrocatalytic Water Oxidation on high-surface-area Spinel $(Cr_{0.2}Mn_{0.2}Fe_{0.2}Co_{0.2}Ni_{0.2})_3O_4$ electrodes," *ACS Applied Energy Materials* 5 (2022): 717–730.

26. T. Brezesinski, B. Smarsly, M. Groenewolt, et al., "The Generation of Mesoporous CeO_2 With Crystalline Pore Walls Using Novel Block Copolymer templates," *Studies in Surface Science and Catalysis* 156 (2005): 243–248.

27. W. Zhou, F. Sun, K. Pan, et al., "Well-ordered Large-pore Mesoporous Anatase TiO_2 With Remarkably High Thermal Stability and Improved Crystallinity: Preparation, Characterization, and Photocatalytic Performance," *Advanced Functional Materials* 21 (2011): 1922–1930.

28. M. Einert, H. Sezen, Q. Wu, et al., "$NiFe_2O_4$ Spinel Thin Film Electrocatalysts: Ordered Mesoporous Networks for Driving the Oxygen Evolution Reaction," *ACS Applied Nano Materials* 8 (2025): 14218–14229.

29. B. Smarsly and M. Antonietti, "Block Copolymer Assemblies as Templates for the Generation of Mesoporous Inorganic Materials and Crystalline Films," *European Journal of Inorganic Chemistry* (2006): 1111–1119.

30. T. E. Quickel, H. van Le, T. Brezesinski, and S. H. Tolbert, "On the Correlation between Nanoscale Structure and Magnetic Properties in Ordered Mesoporous Cobalt Ferrite ($CoFe_2O_4$) Thin Films," *Nano Letters* 10 (2010): 2982–2988.

31. A. Thomas, H. Schlaad, B. Smarsly, and M. Antonietti, "Replication of Lyotropic Block Copolymer Mesophases Into Porous Silica by Nanocasting: Learning About Finer Details of Polymer Self-assembly," *Langmuir* 19 (2003): 4455–4459.

32. Q. Wu, A. Alkemper, S. Lauterbach, J. P. Hofmann, and M. Einert, "Fabrication of Nanocrystalline High-entropy Oxide $CoNiFeCrMnO_x$ Thin Film Electrodes by Dip-coating for Oxygen Evolution Electrocatalysis," *Energy Advances* 3 (2024): 765–773.

33. S. T. Hyde, "Identification of Lyotropic Liquid Crystalline Mesophases," in *Handbook of Applied Surface and Colloid Chemistry*, Vol. 2 (John Wiley & Sons (Wiley), 2001), 299–332.

34. M. Einert, A. Waheed, D. C. Moritz, et al., "Mesoporous $CuFe_2O_4$ Photoanodes for Solar Water Oxidation: Impact of Surface Morphology on the Photoelectrochemical Properties," *Chemistry–A European Journal* 29 (2023) 202300277.

35. S. M. Disseler, J. A. Borchers, C. M. Brooks, et al., "Magnetic Structure and Ordering of Multiferroic Hexagonal $LuFeO_3$," *Physical Review Letters* 114 (2015): 217602.

36. B. M. Gatehouse, S. E. Livingstone, and R. S. Nyholm, "Infrared Spectra of some Nitrato-co-ordination Complexes," *Journal of the Chemical Society (Resumed)* 847 (1957): 4222–4225.

37. A. Małecki, R. Gajerski, S. Łabuś, B. Prochowska-Klisch, and K. Wojciechowski, "Mechanism of Thermal Decomposition of D-metals Nitrates Hydrates," *Journal of Thermal Analysis and Calorimetry* 60 (2000): 17–23.

38. K. C. Patil, R. K. Gosavi, and C. N. R. Rao, "Infrared Spectra and Thermal Decomposition of Metal Nitrites and Nitrates," *Inorganica Chimica Acta* 1 (1967): 155–160.

39. J. Jiu, K. Kurumada, F. Wang, and L. Pei, "Syntheses of Highly Ordered Mesoporous Silica by New Hybrid Template," *Materials Chemistry and Physics* 86 (2004): 435–439.

40. Q. Wu, M. Mellin, S. Lauterbach, et al., "Soft-templated, Mesoporous Co_3O_4 Thin Films for Electrocatalysis of the Oxygen Evolution Reaction," *Materials Advances* 5 (2024): 2098–2109.

41. E. Erdös and H. Altorfer, "Ein Dem Malachit Ähnliches Basisches Eisenkarbonat Als Korrosionsprodukt von Stahl," *Materials and Corrosion* 27 (1976): 304–312.

42. R. P. Turcotte, J. O. Sawyer, and L. Eyring, "Rare Earth Dioxymonocarbonates and Their Decomposition," *Inorganic Chemistry* 8 (1969): 238–246.

43. J.-C. Grivel, "Thermal Decomposition of Lutetium Propionate," *Journal of Analytical and Applied Pyrolysis* 89 (2010): 250–254.

44. J. Vermette, S. Jandl, A. A. Mukhin, et al., "Raman Study of the Antiferromagnetic Phase Transitions in Hexagonal $YMnO_3$ and $LuMnO_3$," *Journal of Physics: Condensed Matter* 22 (2010): 356002.

45. M. Einert, R. Ostermann, T. Weller, et al., "Hollow α-Fe_2O_3 Nanofibres for Solar Water Oxidation: Improving the Photoelectrochemical Performance by Formation of α-Fe_2O_3/ITO-composite Photoanodes," *Journal of Materials Chemistry A* 4 (2016): 18444–18456.

46. C. Suchomski, D. J. Weber, P. Dolcet, et al., "Sustainable and Surfactant-free High-throughput Synthesis of Highly Dispersible Zirconia Nanocrystals," *Journal of Materials Chemistry A* 5 (2017): 16296–16306.

47. H. Fukumura, N. Hasuike, H. Harima, et al., "Spin-coupled Phonons in Multiferroic $YbMnO_3$ Epitaxial Films by Raman Scattering," *Journal of Physics: Conference Series* 92 (2007): 012126.

48. H. Fukumura, S. Matsui, H. Harima, et al., "Raman Scattering Studies on Multiferroic $YMnO_3$," *Journal of Physics: Condensed Matter* 19 (2007): 365239.

49. J. Liu, C. Toulouse, P. Rovillain, et al., "Lattice and Spin Excitations in Multiferroic h-$YbMnO_3$," *Physical Review B—Condensed Matter and Materials Physics* 86 (2012) 184410.

50. J. Vermette, S. Jandl, and M. M. Gospodinov, "Raman Study of Spin–phonon Coupling in $ErMnO_3$," *Journal of Physics: Condensed Matter* 20 (2008): 425219.

51. L. Korell, S. Lauterbach, J. Timm, et al., "On the Structural Evolution of Nanoporous Optically Transparent CuO Photocathodes Upon Calcination for Photoelectrochemical Applications," *Nanoscale Advances* 6 (2024): 2875–2891.

52. A. Hagfeldt and M. Graetzel, "Light-induced Redox Reactions in Nanocrystalline Systems," *Chemical Reviews* 95 (1995): 49–68.

53. V. V. Pavlov, A. R. Akbashev, A. M. Kalashnikova, et al., "Optical properties and electronic structure of multiferroic hexagonal orthoferrites $RFeO_3$ (R= Ho, Er, Lu)," *Journal of Applied Physics* 111 (2012).

54. W. Wang, H. Wang, X. Xu, et al., "Crystal Field Splitting and Optical Bandgap of Hexagonal $LuFeO_3$ Films," *Applied Physics Letters* 101 (2012): 241907.

55. D. M. Sherman, "The Electronic Structures of Fe^{3+} Coordination Sites in Iron Oxides: Applications to Spectra, Bonding, and Magnetism," *Physics and Chemistry of Minerals* 12 (1985): 161–175.

56. H. Das, A. L. Wysocki, Y. Geng, W. Wu, and C. J. Fennie, "Bulk Magnetoelectricity in the Hexagonal Manganites and Ferrites," *Nature Communications* 5 (2014): 2998.

57. W. Kohn and L. J. Sham, "Self-consistent Equations Including Exchange and Correlation Effects," *Physical Review* 140 (1965): A1133.

58. C. Lohaus, A. Klein, and W. Jaegermann, "Limitation of Fermi Level Shifts by polaron Defect States in Hematite Photoelectrodes," *Nature Communications* 9 (2018): 4309.

59. H. Han, D. Kim, S. Chae, et al., "Switchable Ferroelectric Photovoltaic Effects in Epitaxial h-$RFeO_3$ Thin Films," *Nanoscale* 10 (2018): 13261–13269.

60. B. S. Holinsworth, D. Mazumdar, C. M. Brooks, et al., "Direct Band Gaps in Multiferroic h-$LuFeO_3$," *Applied Physics Letters* 106 (2015): 082902.

61. A. T. Melo, D. Brito, A. F. Lima, and M. V. Lalic, "Non-collinear Spin DFT Study of the Ground state Magnetic Structure, Optical and Electronic Properties of the Hexagonal $LuFeO_3$ Multiferroic," *Journal of Alloys and Compounds* 813 (2020): 152227.

62. S. Li, Y. Li, M. Bäumer, and L. V. Moskaleva, "Assessment of PBE+U and HSE06 Methods and Determination of Optimal Parameter U for the Structural and Energetic Properties of Rare Earth Oxides," *Journal of Chemical Physics* 153 (2020): 164710.

63. C. Reitz, C. Suchomski, J. Haetge, et al., "Soft-templating Synthesis of Mesoporous Magnetic $CuFe_2O_4$ Thin Films With Ordered 3D Honeycomb Structure and Partially Inverted Nanocrystalline Spinel Domains," *Chemical Communications* 48 (2012): 4471–4473.

64. A. N. Mansour and R. A. Brizzolara, "Characterization of the Surface of γ-Fe_2O_3 Powder by XPS," *Surface Science Spectra* 4 (1996): 351–356.

65. O. Polat, M. Coskun, Y. Yildirim, et al., "Variation in the Dielectric and Magnetic Characteristics of Multiferroic $LuFeO_3$ as a Result of Cobalt Substitution at Fe Sites," *Journal of Alloys and Compounds* 963 (2023): 170939.

66. J. P. Espinós, A. R. González-Elipe, and J. A. Odriozola, "XPS Study of Lutetium Oxide Samples With Different Hydration/Carbonation Degrees as a Function of the Preparation Method," *Applied Surface Science* 29 (1987): 40–48.

67. M. Einert, A. Waheed, S. Lauterbach, et al., "Sol-Gel-Derived Ordered Mesoporous High Entropy Spinel Ferrites and Assessment of Their Photoelectrochemical and Electrocatalytic Water Splitting Performance," *Small* 19 (2023): 2205412.

68. K. Brezesinski, J. Haetge, J. Wang, et al., "Ordered Mesoporous α-Fe_2O_3 (Hematite) Thin-Film Electrodes for Application in High Rate Rechargeable Lithium Batteries," *Small* 7 (2011): 407–414.

69. K. A. Cychosz and M. Thommes, "Progress in the Physisorption Characterization of Nanoporous Gas Storage Materials," *Engineering* 4 (2018): 559–566.

70. T. Moriya, "Anisotropic Superexchange Interaction and Weak Ferromagnetism," *Physical Review* 120 (1960): 91–98.

71. I. Dzyaloshinsky, "A Thermodynamic Theory of "Weak" Ferromagnetism of Antiferromagnetics," *Journal of Physics and Chemistry of Solids* 4 (1958): 241–255, https://doi.org/10.1016/0022-3697(58)90076-3.

72. F. J. Morin, "Magnetic Susceptibility of αFe_2O_3 and αFe_2O_3 with Added Titanium," *Physical Review* 78 (1950): 819–820, https://doi.org/10.1103/PhysRev.78.819.2.

73. A. J. Kurtzig, R. Wolfe, R. C. LeCraw, and J. W. Nielsen, "Magneto-Optical Properties Of A Green Room-Temperature Ferromagnet: $FeBO_3$" *Applied Physics Letters* 14(1969): 350–352, https://doi.org/10.1063/1.1652682.

74. D. Treves, "Magnetic Studies of some Orthoferrites," *Physical Review* 125 (1962): 1843–1853, https://doi.org/10.1103/PhysRev.125.1843.

75. Y. K. Jeong, J.-H. Lee, S.-J. Ahn, and H. M. Jang, "Epitaxially Constrained Hexagonal Ferroelectricity and Canted Triangular Spin Order in $LuFeO_3$ Thin Films," *Chemistry of Materials* 24 (2012): 2426–2428, https://doi.org/10.1021/cm300846j.

76. T. Katsufuji, S. Mori, M. Masaki, Y. Moritomo, N. Yamamoto, and H. Takagi, "Dielectric and Magnetic Anomalies and Spin Frustration in Hexagonal $RMnO_3$ (R=Y, Yb, and Lu)," *Physical Review B* 64 (2001): 104419, https://doi.org/10.1103/PhysRevB.64.104419.

Supporting Information

Additional supporting information can be found online in the Supporting Information section.

Supporting file: admi70361-sup-0001-SuppMat.docx